

See discussions, stats, and author profiles for this publication at: <https://www.researchgate.net/publication/267391646>

Manganese in Graphite Anode and Capacity Fade in Li Ion Batteries

ARTICLE in THE JOURNAL OF PHYSICAL CHEMISTRY C · OCTOBER 2014

Impact Factor: 4.77 · DOI: 10.1021/jp507833u

CITATIONS

6

READS

114

7 AUTHORS, INCLUDING:



[Arthur Jeremy Kropf](#)

Argonne National Laboratory

186 PUBLICATIONS 2,984 CITATIONS

SEE PROFILE



[Timothy W Marin](#)

Benedictine University

54 PUBLICATIONS 811 CITATIONS

SEE PROFILE



[Oleg G Poluektov](#)

Argonne National Laboratory

86 PUBLICATIONS 1,412 CITATIONS

SEE PROFILE



[Daniel P. Abraham](#)

Argonne National Laboratory

148 PUBLICATIONS 3,261 CITATIONS

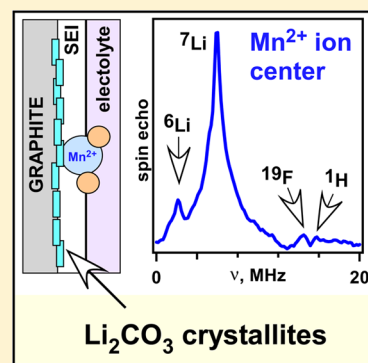
SEE PROFILE

Manganese in Graphite Anode and Capacity Fade in Li Ion Batteries

Ilya A. Shkrob,^{*,†} A. Jeremy Kropf,[†] Timothy W. Marin,^{†,‡} Yan Li,[†] Oleg G. Poluektov,[†] Jens Niklas,[†] and Daniel P. Abraham^{*,†}[†]Chemical Sciences and Engineering Division, Argonne National Laboratory, 9700 South Cass Avenue, Argonne, Illinois 60439, United States[‡]Chemistry Department, Benedictine University, 5700 College Road, Lisle, Illinois 60532, United States

S Supporting Information

ABSTRACT: Improving the stability of Li ion electricity storage devices is important for practical applications, including the design of rechargeable automotive batteries. Many promising designs for such batteries involve positive electrodes that are complex oxides of transition metals, including manganese. Deposition of this Mn on the graphite negative electrode is known to correlate with gradual capacity fade [by increasing retention of lithium cations in the solid electrolyte interphase (SEI)] in Li ion batteries. This SEI contains partially reduced and fully mineralized electrolyte, in the outer (organic) and inner (mineral) layers. In this study, we explore structural aspects of this Mn deposition via a combination of electrochemical, X-ray absorption, and electron paramagnetic resonance experiments. We confirm previous observations that suggest that on a *delithiated* graphite electrode Mn is present as Mn^{2+} ion. We show that these Mn^{2+} ions are dispersed: there are no Mn-containing phases, such as MnF_2 , MnO , or MnCO_3 . These isolated Mn^{2+} ions reside at the surface of lithium carbonate crystallites in the inner SEI layer. For a *lithiated* graphite electrode, there is reduction of these Mn^{2+} ions to an unidentified species different from atomic, nanometer scale or mesoscale $\text{Mn}(0)$ clusters. We suggest that Mn^{2+} ions are transported from the positive electrode to the graphite electrode as complexes in which the cation is chelated by carboxylate groups that are products of electrolytic breakdown of the carbonate solvent. This complex is sufficiently strongly bound to avoid cation exchange in the outer SEI and thereby reaches the inner (mineral) layer, where the Mn^{2+} ion is chemisorbed at the surface of the carbonate crystallites. We conjecture that stronger chelation can prevent deposition of Mn^{2+} ions and in this way retard capacity fade. This action might account for the protective properties of certain battery additives.



1. INTRODUCTION

Positive electrode materials, such as spinel LiMn_2O_4 and olivine LiFePO_4 , are commonly used in rechargeable Li ion batteries.¹ Despite their practical uses, one of the detrimental processes occurring in such batteries is a gradual loss of iron and manganese from the electrode material. This loss occurs during electrochemical cycling, and it has been linked to capacity fade, which includes increased retention of Li^+ ions on the graphite electrode.^{2–12} Similar behavior is observed when manganese salts, such as MnSO_4 or $\text{Mn}(\text{ClO}_4)_2$, are intentionally added to the electrolyte.^{12,13}

Understanding the dissolution, transport, and deposition of transition metals is particularly important in automotive and grid applications, due to the long life requirements of these electricity storage devices; slow deterioration of their performance is problematic. In this study, we examine the structural and mechanistic aspects of manganese dissolution processes in cells with $\text{Li}_{1.2}\text{Ni}_{0.15}\text{Mn}_{0.55}\text{Co}_{0.1}\text{O}_2$ as the positive electrode, graphite as the negative electrode, and organic carbonates containing LiPF_6 as the electrolyte.

One of our motivations is harmonizing different opinions that have emerged from previous research, as there is an ongoing discussion regarding the oxidation state of Mn on the

graphite electrode. The surface of this electrode is covered by solid deposits of breakdown products that are generated via electrochemical reduction of the solvent and hexafluorophosphate anions (solid electrolyte interphase, SEI).^{14–18} The SEI is often described as having a multilayer structure: a mineralized inner layer (a matrix consisting of nanosized crystalline grains of lithium carbonate, fluoride, and oxalate that are the final products of electrolyte decomposition) and a thicker (10–30 nm) organic (likely polymeric) material.^{18,19} This organic material forms a soft, porous outer layer, where the electrolyte reduction is incomplete.^{20,21} It has been suggested that Mn is present as metallic $\text{Mn}(0)$ nanoparticles that provide a conductive path for the electrons through the (largely insulating) SEI, resulting in excessive electrolyte breakdown. This more efficient reduction process yields breakdown products that contain carboxylate groups such as ethylene dicarbonate. These products associate with Li^+ ions, causing their retention in the SEI, so fewer Li^+ ions can migrate back to the cathode during the graphite-delithiation cycle. An

Received: August 3, 2014

Revised: September 29, 2014

Published: October 1, 2014

alternative view is that the Mn^{2+} ions become embedded in the SEI and serve as catalytic centers for electrolyte decomposition.¹³ There are observations that favor both views; furthermore, the two scenarios are not mutually exclusive.

Delacourt et al.²² proposed two-electron reduction of solvated Mn^{2+} to $\text{Mn}(0)$ clusters at the electrode and the subsequent oxidation of these metallic clusters by the electrolyte to MnCO_3 . Ochida et al.¹¹ suggested that this oxidation step occurs under open-circuit conditions (presumably 3 V vs Li/Li^+) and involves an unspecified Mn^{2+} solid phase. However, this postulated metallic phase was not found when using X-ray absorption spectroscopy.²² Mn L-edge soft X-ray spectra suggested only the occurrence of Mn^{2+} ions, and their coordination environment was intermediate between those of two reference compounds, MnO and MnCO_3 .²² From a comparison of edge positions in their X-ray absorption spectra (XAS), Zhan et al.¹ inferred that predominantly Mn^{2+} ions are present on the negative electrode, regardless of the electrode potential, which is also contrary to the $\text{Mn}(0)$ scenario.^{3–7,11} Their EXAFS (extended X-ray absorption fine structure) spectra suggested that the Mn^{2+} ion is coordinated by six O^{2-} anions with Mn–O bond length of 2.15 ± 0.03 Å; Mn 2p X-ray photoelectron spectra (XPS) were also consistent with such oxygen-coordinated Mn^{2+} ions. Neither the XANES (X-ray absorption near-edge) nor EXAFS spectra were consistent with the MnCO_3 phase that was postulated by Delacourt et al.²²

In minerals, Mn^{2+} ion is typically octahedrally coordinated. The pre-edge feature in XANES spectra observed for Mn compounds originates through electronic transitions from the 1s core levels to the empty 3d levels hybridized by the ligands, and it is observed in all of the oxidation states of manganese.^{23,24} Terada et al.¹⁰ used XAS to show that the pre-edge feature in XANES spectra of *electrolyte* fluid corresponds to Mn^{2+} ; however, there was extensive processing of the sample prior to the measurement, which can change the oxidation state. Their attribution would be consistent with the hypothesis that Mn is transported across the electrochemical cell and deposited in the SEI as Mn^{2+} ion. Han et al.²⁵ have suggested that this ion drifts along the electric field as a $[\text{MnL}_4]^{2+}$ cation that is coordinated by four (neutral) ethylene carbonate molecules (L) in a manner similar to $[\text{LiL}_4]^+$ ion. The corresponding $[\text{ML}_4]^0$ complexes (where M = Mn, Co, Ni) would be relatively unstable to inner sphere oxidation to M^+ concerted with the ring opening in the carbonate ligand (L), yielding $\text{L}_3\text{M}^+[\text{O}_2\text{COCH}_2\cdot\text{CH}_2]$. Their computations indicate that $\text{Mn}(0)$ induces ring-opening decomposition of the ethylene carbonate (EC) solvent; this reaction is slightly exothermic. This study suggests that *isolated* $\text{Mn}(0)$ centers would be unstable in contact with the carbonate electrolyte.

In contrast, Xiao et al.²⁶ reported direct observations of $\text{Mn}(0)$ and MnF_2 nanoparticles (ca. 20 nm) using electron microscopy and XPS. Even larger $\text{Mn}(0)$ particles (100–400 nm) were reported by Ochida et al.,¹¹ who used atomic force microscopy to examine highly oriented pyrolytic graphite. The latter group observed a systematic shift in the electron binding energies for Mn 2p and 3s peaks in the XPS spectra obtained under open-circuit conditions (presumably 3 V vs Li/Li^+), which suggests ongoing oxidation of $\text{Mn}(0)$ to Mn^{2+} as the metallic clusters reduce the electrolyte. From examination of the X-ray absorption near edge spectroscopy (XANES) features, Gowda et al.²⁷ confirmed the presence of $\text{Mn}(0)$ on graphite particles in the negative electrode. However, neither

Mn metal foil nor organometallic Mn^+ carbonyls provided a good fit to the observed X-ray absorption spectra.

Taken together, these observations do not yet add up to present a coherent picture. From a methodological perspective, the use of high fluxes of X-rays and electrons for structural analyses may induce undesired changes in the oxidation state of Mn in the SEI. Furthermore, this state may depend on the condition of the graphite electrode, as the reductive potential of the surface changes with the degree of lithiation; it is conceivable that different Mn oxidation states prevail during different parts of the electrochemical cycle. Gowda et al.²⁷ studied several cells under different cycling conditions using 200 ppm Mn^{2+} in the electrolyte. These authors observed that XANES for such samples were similar to the spectra collected for samples in which Mn^{2+} was introduced through electrochemical cycling (i.e., the positive electrode dissolution). When care was taken to maintain the sample in the reduced state, all of their XANES spectra were qualitatively different from the ones obtained by Zhan et al.¹ (However, the sample that was washed with an excess of DMC showed an oxidized Mn XANES that was qualitatively similar to that of Zhan et al.¹) A notable change in their experimental protocol vis-à-vis Zhan et al.¹ was that before harvesting of the electrode, the cell was held at 4.6 eV until the current decayed; i.e., the graphite electrode was in the fully *lithiated* state. That is, reduced Mn is observed in XANES spectra when the graphite electrode is harvested in the lithiated state and careful sample preparation procedures are followed.²⁷ The authors explicitly note the need to examine the graphite anode at low potentials to capture the nature of any possible reduced Mn species; oxidation of the Mn occurs when the aforementioned conditions are not met. Indeed, the results of Ochida et al.¹¹ had already indicated that reduced Mn is inherently unstable and transforms to a higher oxidation state given sufficient time.

In this study, we complement electrochemical studies and XAS observations with noninvasive spectroscopic techniques: continuous wave (cw) and pulsed electron paramagnetic spectroscopy (EPR). Mn^{2+} is an open-shell d^5 ion that has a distinct EPR signature.²⁸ Furthermore, $\alpha\text{-Mn}(0)$, MnCO_3 , MnO , and MnF_2 are paramagnetic phases at room temperature that become antiferromagnetic at lower temperature with characteristic phase transitions that are observable using EPR. These properties allow us to demonstrate that Mn is present only as magnetically isolated Mn^{2+} ions on *delithiated* graphite electrodes. Electron spin echo envelope modulation (ESEEM) spectroscopy was used to observe nuclear spin transitions in magnetic nuclei (^6Li , ^{19}F , ^1H) around the ion and to establish the second shell structure, complementing the previous XAS data regarding the first coordination shell. These measurements allow us to establish the structural model of the Mn^{2+} ion center.

Our results suggest that the final destination of Mn in the SEI of *delithiated* graphite electrodes is formation of *dispersed* Mn^{2+} ions embedded in a mineral phase, most likely lithium carbonate crystallites. We discuss the mechanisms for dissolution, transport, and deposition of Mn^{2+} ions that are consistent with these structural observations. Furthermore, we show that the state of Mn on a lithiated graphite electrode is different from the one on a delithiated electrode. On the lithiated electrodes we observe in the XANES spectra the pre-edge features that Gowda et al.²⁷ attributed to $\text{Mn}(0)$, while the EPR signature of Mn^{2+} ions is absent. However, our EPR examinations failed to reveal the anticipated features of α -

Mn(0) nanoparticles in such samples. More generally, there is no evidence for paramagnetic and antiferromagnetic (nano)-phases. Furthermore, close examination of the EXAFS patterns indicates that the reduced Mn species on the lithiated graphite electrode does not arise from clusters of a few Mn(0) atoms or metallic particles.

To save space, many of the supporting tables and figures, details of synthetic and analytical protocols, and a list of abbreviations have been placed in the Supporting Information (SI). When referenced in the text, these materials have the designator "S", as in Figure 1S.

2. EXPERIMENTAL AND COMPUTATIONAL METHODS

2.1. Materials. The positive and negative electrodes used in this study were fabricated in Argonne's Cell Analysis, Modeling and Prototyping (CAMP) facility.²⁹ The positive electrode contained $\text{Li}_{1.2}\text{Ni}_{0.15}\text{Mn}_{0.55}\text{Co}_{0.1}\text{O}_2$ (Toda HE5050), carbon black (Timcal SuperP Li), and PVdF (Solvay 5130). The negative electrode contained graphite (Philips 66 A12, 10 μm size, 3 m^2/g surface area), carbon black (Timcal SuperP Li, 4 wt %, 45 m^2/g surface area), and PVdF binder (Kureha KF9300, 6 wt %). The electrolyte contained 1.2 M LiPF_6 in a 3:7 w/w liquid mixture of ethylene carbonate (EC) and ethyl methyl carbonate (EMC). Metallic Mn(0) spheres were obtained from Aldrich (50 mesh, 300 μm particles). A nanopowder (30–50 nm α -Mn(0) with a 10 nm thick outer shell of Mn_3O_4 , 99.9% metal base) synthesized with the procedure in ref 30 was obtained from American Elements (item MN-M-03M-NP.030N). All other reagents and materials described in the paper were obtained from Aldrich in their purest form.

2.2. Electrochemical Cycling. Electrochemical cycling was conducted in 2032-type coin cells, with 1.6 cm^2 area electrodes, assembled in an Ar-atmosphere glovebox. The data reported in this paper are from cells that were operated for 200 cycles between 2.2 and 4.6 V at 55 °C. The cells were held at constant voltage, either at 2.0 or 4.6 V, for 48 h before harvesting the electrodes. At 2.0 and 4.6 V, the graphite electrode is mainly in the delithiated and lithiated states, respectively; the electrode potential, determined from separate measurements, is ~ 1.4 and ~ 0.070 V vs Li/Li^+ , respectively. The electrodes were either lightly washed with dimethyl carbonate (DMC) or examined in the as-harvested (no wash) condition. Typical cycling data from our electrochemical experiments are shown in Figure 1S (SI). The ~ 4.4 V pseudoplateau in the first charge cycle is attributed to electrochemical activation of the oxide; all successive cycles displayed sloping capacity–voltage profiles. The discharge capacities, measured at 55 °C with a 15 $\text{mA}/\text{g}_{\text{oxide}}$ current, are ~ 260 and ~ 163 $\text{mAh}/\text{g}_{\text{oxide}}$ for cycles 1 and 204; that is, the cell capacity fade is 37.3%.

Chemical analysis was conducted by inductively coupled plasma–mass spectrometry (ICP-MS) on graphite electrodes scraped off the current collector.² The typical concentrations of Mn were ~ 1000 ppm ($\mu\text{g}/\text{g}$ sample), which is roughly equivalent to one atom per $6.6 \times 6.6 \text{ \AA}^2$ of the graphite electrode surface. In contrast, the liquid electrolyte contained <0.2 ppm Mn, suggesting that at any given moment, the concentration of dissolved Mn is very low; i.e., the deposition occurs from a very dilute solution and is the cumulative result of prolonged aging.

2.3. X-ray Absorption Measurements. Mn K-edge XAS measurements were carried out at the Materials Research Collaborative Access Team (MRCAT) 10-BM-B beamline at Argonne's Advanced Photon Source (APS). A monochromatic

beam was provided by a water-cooled Si(111) double crystal monochromator, and harmonics were attenuated by detuning the crystal alignment to 50% of the peak intensity. The Mn K edge energy was calibrated to a primary fine-powdered, metallic Mn sample or secondarily to a MnO sample that had been calibrated to the same metallic Mn reference. The peak of the first derivative for metallic Mn was assigned to 6537.67 eV. The loss of accuracy for the secondary standard was estimated to be less than ± 0.05 eV.

For XAS measurements, the entire electrode was sealed in a dry Ar-purged glovebox between layers of 50 μm thick Kapton tape, and such sealed samples were doubly bagged in Ar-filled plastic bags and transported in an argon-filled Mason jar to eliminate any possible exposure to air. During the X-ray measurements, the samples were held within one unopened Ar-filled plastic bag. The Mn $K\alpha$ fluorescence emission was detected using a Vortex ME4 four-element silicon-drift detector using XIA XMAP digital signal processing. Multiple 25 min scans were averaged. XAFS data were processed using the *Athena* interface to *ifeffit* and the EXAFS data were analyzed using *Artemis* and *feff* version 8.28.^{31–33}

The quality of these XAS spectra was determined by the time limits on the acquisition of the spectrum imposed by gradual changes in the graphite electrodes that were observed to continue even when these samples were not exposed to the X-rays. These changes were observed on the time scale of hours and continued for days. For the lithiated graphite electrode, the spectrum changed very slightly over the 12 h of measurement, while for the delithiated graphite electrode the changes were sufficiently noticeable so that only the three successive scans collected over 1 h could be averaged. As judged from the progressive increase in the energy of the absorption edge, this slow change is caused by oxidation of Mn. This reaction was observed even when much precaution was taken to avoid contact of the sample with the air, suggesting that the oxidation is an intrinsic property of the system.

2.4. Continuous Wave EPR Spectroscopy. For continuous wave (cw) EPR measurements, the graphite was removed from the collector after harvesting of the electrodes, and the samples were evacuated and flame-sealed in Suprasil quartz glass tubes. Reference compounds were also placed and sealed in these glass sample tubes. The graphite samples were stored in liquid nitrogen to prevent slow redox reactions.

First-derivative cw EPR spectra were observed using a 9.44 GHz Bruker ESP300E spectrometer, equipped with a programmable flow helium cryostat (Oxford Instruments, model CF935). The magnetic field and the hyperfine coupling constants (hfcc's) are given in the units of gauss ($1 \text{ G} = 10^{-4} \text{ T}$). If not stated otherwise, the first-derivative EPR spectra were obtained using 2 mW of microwave power and 2 G modulation at 100 kHz. Importantly, even the original electrode material contained significant paramagnetic impurities. There is a narrow line (Figure 2S, SI) from carbon dangling bond (C db) centers with principal g -tensor values of 2.036 (g_{\parallel}) and 2.006 (g_{\perp}). This EPR signal obscures the $m_I = \pm 1/2$ resonance lines of the Mn^{2+} ion center (see section 3.2). In addition to this C db center resonance, there is also a broad line (Figure 3S, SI) stretching over 5 kG that originates from a transition metal impurity, which is likely to be from the 5 ppm iron in SuperP carbon black (section 2.1). Due to rapid spin relaxation in this impurity center, these species are not observed in pulsed EPR, as the electron spin echo signal of this center decays within the dead time of the EPR spectrometer.

2.5. Pulsed EPR Spectroscopy. Pulsed EPR spectra and kinetics were obtained using a Bruker ELEXSYS E580 EPR spectrometer (Bruker Biospin) equipped with a 1 kW traveling-wave tube amplifier (Applied Systems Engineering). A Flexline dielectric ring resonator (Bruker EN 4118X-MD4-W1) was used. Cryogenic temperatures were achieved with a helium gas-flow cryostat. Primary and stimulated electron spin echo (pESE and sESE, respectively) were obtained using $90^\circ\text{--}\tau\text{--}180^\circ\text{--}\tau$ and $90^\circ\text{--}\tau\text{--}90^\circ\text{--}T\text{--}90^\circ\text{--}\tau$ microwave pulse sequences, respectively; the flip angle of 90° corresponds to a 12 ns pulse; the dead time of the spectrometer was 120 ns. The appropriate phase cycling was used to suppress unwanted spin echoes. The initial data processing was done using Xepir software (Bruker BioSpin).

The magnetic dipole interaction of unpaired electron with magnetic nuclei in the matrix causes modulation of the envelope (ESEEM) of the primary (p-) and stimulated (s-) echo as a function of the time intervals τ and T (for fixed τ) between the microwave pulses.³⁴ Modulus Fourier transform (FT) of these time domain traces yields frequency domain ESEEM spectra that are an analog of nuclear magnetic resonance (NMR) spectra for paramagnetic centers, in which the nuclear spin transitions are indirectly observed via the electron spin transitions.

For an $S = 1/2$ system, there are two NMR frequencies, ν_α and ν_β , corresponding to the up and down orientation of the electron spin relative to the magnetic field, B_0 , of the EPR spectrometer. For a distant (weakly coupled) nucleus in a matrix, $\nu_\alpha \approx \nu_\beta \approx \nu$, where ν is the Larmor frequency for a free nucleus. It can be shown that pESEEM and sESEEM spectra are dominated by these $\nu_{\alpha,\beta}$ resonances, while pESEEM spectra also exhibit combined $\nu_\alpha + \nu_\beta$ modes. The decay rate of the pESE kinetics in the τ -domain is determined by the transverse relaxation time for the electron spin (T_2), whereas the decay of the sESE kinetics in the T -domain is determined by the slower longitudinal relaxation ($T_1 \gg T_2$). A longer sampling interval for the latter (due to the slower decay of the echo signal) makes the sESEEM spectra better resolved in the frequency domain as compared to the pESEEM ones; these sESEEM spectra are also easier to interpret. The additional advantage of using sESE is in the ability to selectively suppress or enhance contributions from different types of nuclei (with NMR frequency ν), as the amplitude changes as $1 - \cos(2\pi\nu\tau)$. This amplitude can be changed between 0 and 2 by judiciously choosing the delay time τ between the microwave pulses; in this way the modulation induced by a given nucleus can be favored or suppressed. It is noteworthy that the NMR frequencies ν change linearly with the magnetic field B_0 , which introduces predictable changes in the observed modulation frequencies for different components of the spin multiplet (see section 3.4 below).

3. RESULTS

3.1. Mn K-Edge XAS Experiments. As seen from the comparison given in Figure 1a, for an aged delithiated graphite electrode, our XAS spectrum is similar to that reported by Zhan et al.¹ The entire spectrum originates from an Mn^{2+} ion, and the analysis of EXAFS yielded the same octahedrally coordinated species with the reported bond distances. Thus, the same species was studied by these previous researchers and in our EPR experiments (see below).

In contrast, XAS spectra obtained from freshly harvested lithiated electrodes (Figure 1b) were strikingly similar to the

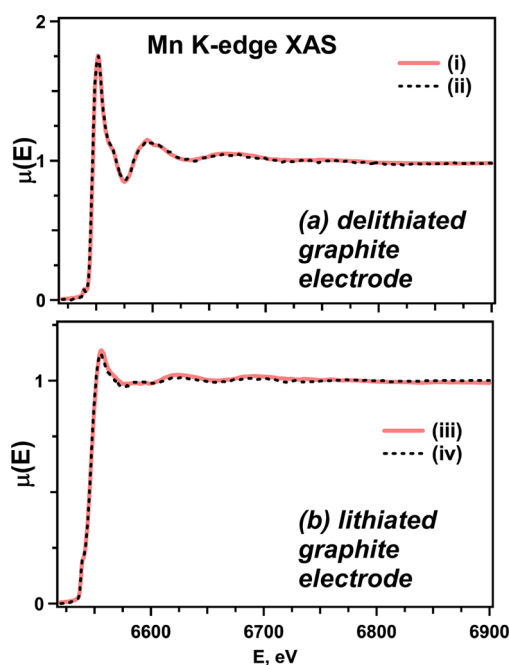


Figure 1. Manganese K-edge X-ray absorption spectra for Mn deposited in graphite electrodes. Traces i and iii were obtained from the delithiated and lithiated graphite electrodes, as explained in the experimental section. Traces ii and iv (broken lines) are XAS spectra from refs 1 and 27, respectively.

ones reported by Gowda et al.,²⁷ and they were distinctly different from the ones reported by Zhan et al. for graphitic electrodes.¹ As explained in the Introduction, Gowda et al. interpreted these XAS spectra as originating from zerovalent Mn with some quantity of oxidized Mn; indeed, the pronounced pre-edge feature and the edge position in XANES support this interpretation. However, in section 3.7 we present EXAFS analysis that appears to exclude $\text{Mn}(0)$ clusters or particles in the samples. EPR spectroscopy results discussed in section 3.3 lead to the same conclusion and will be presented first.

We conclude therefore that (at least some) Mn^{2+} ions become reduced during the *lithiation* stage of the cycle and that this reduced Mn is oxidized to Mn^{2+} during the *delithiation* stage.

3.2. Continuous Wave EPR Spectroscopy of Mn^{2+} Ion Center. ^{55}Mn is a naturally occurring magnetic nucleus with spin $I = 5/2$ (100% natural abundance); Mn^{2+} is an $S = 5/2$ ion with g -factor close to 2. Trace i of Figure 2 shows the typical cw EPR spectrum of a delithiated graphite electrode (section 2.2) at room temperature. The narrow resonance line at the center is from a C dangling bond defect on the (delithiated or lithiated) graphite (section 2.4 and Figure 2S, SI). In the magnified spectral wings, there are four resolved lines (indicated by arrows in the plot) that correspond to $m_I = \pm 3/2$ and $\pm 5/2$ transitions in $^{55}\text{Mn}^{2+}$ ion with the isotropic hfcc $a_{\text{iso}} \approx 100$ G. For comparison, at the top we placed the EPR spectra obtained from (i) Mn^{2+} -doped SrO spinel and (ii) $\text{Mn}(\text{II})$ acetate in water–ethylene glycol glass. At 10 K, the narrow line of the C db center becomes less prominent due to microwave saturation of the corresponding spin transition, and the $m_I = \pm 1/2$ lines of the Mn^{2+} ion are also observed (Figure 3).

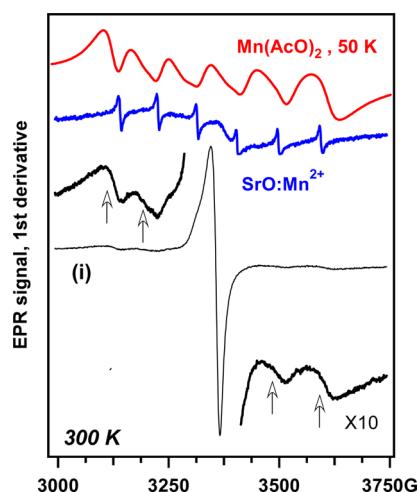


Figure 2. First-derivative cw EPR spectrum of the delithiated graphite electrode (trace i obtained at 300 K). The arrows in the magnified wings of the spectrum ($\times 10$) indicate $m_I = \pm 3/2, \pm 5/2$ lines of $^{55}\text{Mn}^{2+}$, and the narrow line at the center is a carbon dangling bond center in graphite. For comparison, at the top we juxtapose EPR spectra of Mn(II) in $\text{SrO}:\text{Mn}^{2+}$ solid matrix and Mn(II) acetate in frozen glassy water/ethylene glycol solution at 50 K.

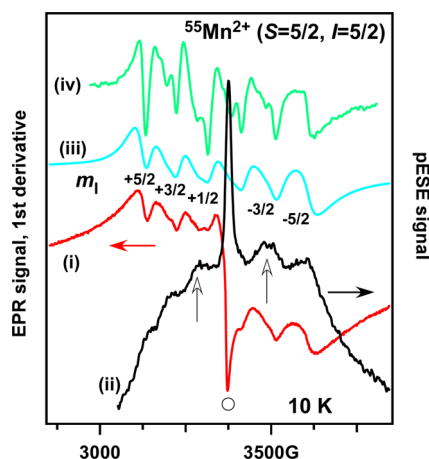


Figure 3. First-derivative cw EPR spectrum of delithiated graphite electrode from Figure 2 obtained at 10 K (trace i, to the left). The projections m_I of the nuclear spin for individual lines of the hyperfine multiplet for $^{55}\text{Mn}^{2+}$ are indicated. Trace ii (to the right) is the primary spin echo signal for $\tau = 120$ ns. The narrow signal at the center (indicated by the open circle in trace i) is from the carbon dangling bond center in graphite, and this signal is in partial microwave saturation in the cw EPR spectrum (trace i). The arrows indicate the $m_I = \pm 1/2$ lines used for spin echo experiments. Traces iii and iv (to the right) are first-derivative EPR spectra of Mn(II) acetate in frozen aqueous ethylene glycol glass and glacial acetic acid, respectively. The additional structure originates through zero-field splitting interactions.

For Mn^{2+} ion, all allowed $(M_S, m_I) \leftrightarrow (M_S + 1, m_I)$ transitions ($M_S = -S, \dots, +S$) contribute to the resonance line at $g \approx 2$. As high-spin ions exhibit a nonvanishing ZFS (zero-field or spin–spin splitting) tensor (i.e., the corresponding spin Hamiltonian includes an $\mathbf{S} \cdot \mathbf{D} \cdot \mathbf{S}$ term), the corresponding spectral contributions are different, with most of the 6-line structure ($m_I = -I, \dots, +I$) originating from the spin-allowed $M_S = -1/2 \leftrightarrow M_S = +1/2$ transitions. The additional structure (that can also be observed in cw EPR spectra from Mn^{2+} in aqueous ethylene glycol glass and glacial acetic acid) originates from the

ZFS interaction with $D \sim -0.5$ GHz (see Figure 3 in ref 28). Since the resolution of our EPR spectra for Mn^{2+} ions in delithiated graphite electrode was poor, it was impossible to determine this ZFS tensor, whereas ESEEM analysis for $S > 1/2$ systems generally requires inclusion of such spin–spin interactions.^{28,35,36} The corrections due to this ZFS interaction are the lowest for the central $-1/2 \leftrightarrow +1/2$ transition²⁸ (see trace ii in Figure 3), so we optimized the microwave pulses for these two resonance lines and treated the spin system as an $S' = 1/2$ Kramers doublet.

We emphasize that this cw EPR spectrum clearly originates from *magnetically dispersed* Mn^{2+} ions, as there is no indication of dipole–dipole or Heisenberg exchange interactions between these Mn^{2+} ions (section 3.3). Figure 4S (SI) exhibits cw EPR spectra obtained over 5 kG between 10 and 300 K. In addition to C db and Mn^{2+} ion centers, there are broad resonance lines from the paramagnetic impurity mentioned in section 2.4 (Figure 3S, SI). An important question is whether there are additional resonances from Mn-related species, e.g., the postulated MnCO_3 , MnF_2 , and metallic $\text{Mn}(0)$ phases. The structureless resonance lines of these paramagnetic or antiferromagnetic phases can be obscured by the stronger C db and Mn^{2+} resonances. To answer this question, we interpolated the baseline (see Figure 3S, SI) and subtracted it to obtain the corrected EPR spectra shown in Figure 5S (SI). In Figure 4, we normalized these difference EPR spectra to

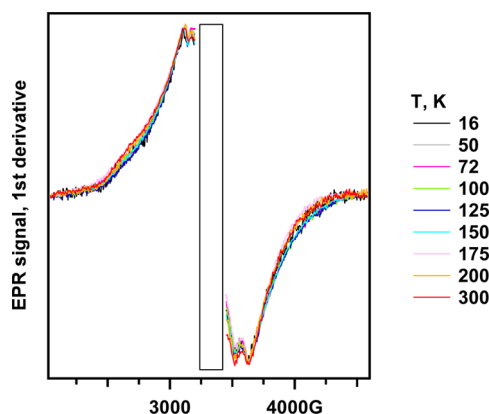


Figure 4. Temperature dependence for the normalized first-derivative cw EPR spectra of $^{55}\text{Mn}^{2+}$ in delithiated graphite electrode. The temperatures are indicated in the plot. These spectra were obtained after background subtraction and normalization as described in Figures 4S and 5S of the SI. The rectangle masks the resonance line from the carbon dangling bond center in graphite.

facilitate their comparison. It is seen from the plot that the spectral envelope does not significantly change as a function of temperature. Below we argue that this observation excludes all of the suggested paramagnetic and antiferromagnetic Mn phases.

Importantly, EPR spectra of lithiated and delithiated samples (that are so different in their X-ray absorption spectra, as exemplified in Figure 1) were qualitatively different. Whereas the delithiated samples yield a readily recognizable spectral signature of Mn^{2+} ions, this signature was entirely absent for the lithiated samples. While this can be expected from the results shown in Figure 1, the complete lack of any Mn-related resonance lines in the lithiated samples is surprising because $\alpha\text{-Mn}(0)$ (nano)phases (postulated to be the reduced Mn species) are paramagnetic, becoming antiferromagnetic at low

temperature. Our EPR experiments, however, indicated that such phases do not occur in either lithiated or delithiated graphite electrodes (section 3.3).

Another noteworthy observation is that the EPR spectra in delithiated samples are identical for graphite electrodes that are paired with $\text{LiNi}_{0.5}\text{Mn}_{1.5}\text{O}_4$ spinel electrodes, and the same species was observed for graphite electrodes cycled at either 30 or 55 °C. These results indicate that in all of the delithiated graphite electrodes, there is only one type of the Mn^{2+} ion center (regardless of the source of Mn) and that this center is dispersed in the SEI matrix.

3.3. The Search for Magnetic Phases. As discussed in the Introduction, several previous authors have suggested that Mn in the SEI forms a new phase. Nanoparticles of $\alpha\text{-Mn}(0)$, MnO , MnF_2 , and MnCO_3 have been suggested as possible candidates for this new phase. All these crystalline phases are paramagnetic above their Néel temperature ($T > T_N$) and become antiferromagnetic at $T < T_N$. As explained above, it is possible that the resonance lines from these magnetic phases either are obscured by the stronger signal from the dispersed Mn^{2+} ions or are so broad that they are not observed. In this section, we demonstrate that such a situation is unlikely.

For $T > T_N$, these phases behave like typical paramagnetic crystals, as the Heisenberg exchange between the ions is overcome by thermal fluctuations. Figure 6S (SI) exhibits the cw EPR spectrum of the typical Mn^{2+} paramagnetic phase, Mn(II) acetate tetrahydrate. These EPR spectra are Lorentzian lines; the line width ΔB_{pp} (the interval between the points of the maximum slope in the first-derivative EPR spectrum) only slightly increases as the temperature decreases (Figure 5, trace

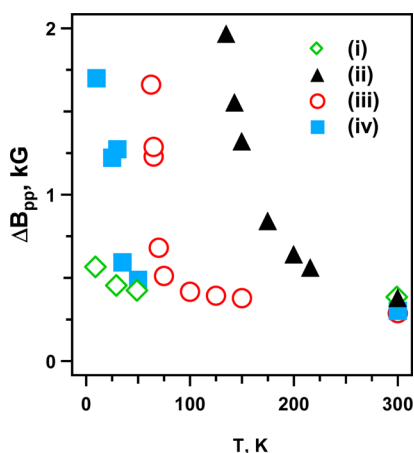


Figure 5. Temperature dependence of the peak-to-peak line width ΔB_{pp} for Mn(II) phases: (i) $\text{Mn(AcO)}_2 \cdot 4\text{H}_2\text{O}$, (ii) MnO , (iii) MnF_2 , and (iv) MnCO_3 . A rapid increase in the line width occurs as the sample temperature T approaches the corresponding T_N .

i). There is no hyperfine coupling (hfc) structure from ^{55}Mn nuclei due to strong magnetic interactions between the electron spins. In Figure 7S (SI), we plot the EPR spectra of MnO powder. The shape of these resonance lines is still Lorentzian, but ΔB_{pp} rapidly increases at the onset of the antiferromagnetic transition at $T_N = 116$ K (Figure 5, trace ii). The same behavior is observed for MnF_2 that has $T_N = 67$ K [Figures 8S (SI) and 5, trace iii]. For MnCO_3 (that has $T_N = 34$ K; see Figure 9S, SI), in addition to this line broadening (Figure 5, trace iv), there is a significant increase in the effective g -factor of the resonance line (g_{eff}). Had any of these phases been present in

the SEI, as the temperature approaches T_N , there would be rapid line broadening (and in some cases g_{eff} shift), so even if their narrow resonance line had been obscured by a stronger resonance line from the dispersed Mn^{2+} ions at $T > T_N$, the broadened signal from the magnetic phase would be observed as T approaches T_N . However, this broadening does not occur, which excludes the presence of all such magnetic phases.

To illustrate how the opposite situation would appear, consider Figure 10S (SI) for a model system, Mn^{2+} -doped Li_2CO_3 . To prepare this sample, a suspension of lithium carbonate in a dilute aqueous solution of Mn(II) acetate was stirred for 2 h at the room temperature; the crystals were filtered and dried in a vacuum at 150 °C. The cw EPR spectrum of this sample exhibits the six-line pattern from dispersed Mn^{2+} ions superimposed onto a broad Lorentzian line that behaves exactly like the feature shown in Figure 9S (SI) for MnCO_3 . Thus, in this system dispersed Mn^{2+} ions coexist with the Mn(II) carbonate phase, and the latter is readily observed using cw EPR. No such resonances were observed in our graphite samples.

An alternative possibility discussed in the literature is the formation of $\text{Mn}(0)$ nanoparticles that were observed using electron transmission microscopy.²⁶ Single-crystal $\alpha\text{-Mn}$ is antiferromagnetic with $T_N = 100$ K.^{37,38} We first examined relatively large 300 μm $\alpha\text{-Mn}(0)$ particles. As seen from Figure 11S (SI), the EPR spectrum consists of two Lorentzian lines corresponding to $g \approx 4$ and $g \approx 2$ transitions (components A and B, respectively, in Figure 11S, SI). The latter correspond to the “forbidden” $M_S \leftrightarrow M_S + 2$ transitions that become allowed due to magnetic dipole coupling between the ions in the metal. It can be seen that the $g \approx 2$ line broadens out (as is the case with other antiferromagnetic materials) as T approaches T_N (Figures 11S and 12S, SI), whereas the $g \approx 4$ line persists; there is also the characteristic increase in g_{eff} (Figure 12S, SI).

We then asked whether the tentative $\text{Mn}(0)$ nanoparticles would exhibit the same behavior as these larger metal particles. Figures 13S–15S (SI) summarize cw EPR spectra obtained for 30–50 nm $\text{Mn}(0)$ nanoparticles coated with 10 nm Mn_3O_4 . The Mn(II,III) oxide becomes ferromagnetic at the Curie temperature $T_C = 43$ K, and there is strong interaction of the two magnetic phases. For $T > T_C$, nanoparticles of Mn_3O_4 (like other paramagnetic Mn oxides) yield a broad Lorentzian line with $g \approx 2$ that becomes extremely broad as T decreases toward T_C ; further lowering of the temperature yields ferromagnetic resonance in a low field.³⁹ Figure 13Sa (SI) (for $T = 100$ –300 K) illustrates this behavior: this EPR spectrum is a composite, with component A ($g \approx 4$) being analogous to the one observed in the bulk metal (Figure 11S, SI); components B and C with $g \approx 2$ are also observed. Component B is a narrow resonance line, whereas component C is broad; it becomes invisible at 100 K, so only components A and B remain (Figure 13Sb, SI). The behavior of component C is consistent with the behavior observed in Mn_3O_4 .³⁹ Between 150 and 75 K, component B narrows as the temperature decreases (Figures 13Sb, 14Sa, and 15S, SI), but below 75 K it broadens once again (Figure 14Sa, SI). The g_{eff} for component A rapidly increases (Figures 14Sb and 15S, SI) around $T = 100$ K, which corresponds to T_N for bulk $\alpha\text{-Mn}(0)$. We attribute component A to the same forbidden transition that was observed in 300 μm metal particles; component B can originate from the metal/oxide interface.

This examination suggests that $\alpha\text{-Mn}(0)$ (nano)particles can be readily fingerprinted through the “forbidden” $g \approx 4$ line

(component A) with the characteristic temperature dependence of g_{eff} . As no such resonance was observed in the EPR spectra of the graphite electrode, whether lithiated or delithiated (see section 3.2), we can exclude such α -Mn(0) 30–50 nm sized phases. Our conclusion is that no magnetic Mn-containing phases are present in the lithiated or delithiated graphite electrodes, despite the XANES features suggesting Mn(0) occurrence. If there are metallic clusters present in the sample, these must be very small diamagnetic clusters; the larger Mn(0) particles reported are likely to be artifacts induced by radiolytic reduction of Mn^{2+} by focused electron beams.²⁶ However, the presence of even small Mn(0) clusters is questionable, as most of such clusters are (super)paramagnetic, with some known exceptions, such Mn_2 and Mn_8 clusters.^{40–42} In section 3.7 we exclude this residual possibility using EXAFS spectroscopy.

3.4. ESEEM Spectroscopy of Dispersed Mn^{2+} Ions.

Figure 6 exhibits primary ESE kinetics observed for $B_0 = 3580$

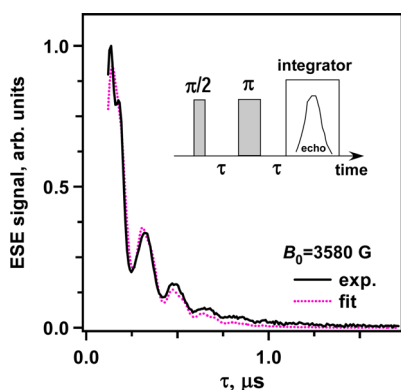


Figure 6. Solid line: primary electron spin echo kinetics for the $m_1 = -1/2$ line (Figure 3). The inset shows the pulse excitation scheme that involves two short microwave pulses with flip angles of 90° and 180° . The dashed line shows the simulated kinetics using the model described in the text.

G (see Figure 3, trace ii). These kinetics exhibit deep modulation at the NMR frequency of ^7Li nuclei, suggesting that the dispersed Mn^{2+} ion magnetically interacts with several nearby Li^+ cations. We remind the reader that Li has two naturally abundant magnetic isotopes, ^6Li ($I = 1$, 7.6 atom % abundance) and ^7Li ($I = 3/2$, 92.4 atom % abundance); other magnetic isotopes in the system include ^{19}F ($I = 1/2$), ^1H ($I = 1/2$), and ^{31}P ($I = 1/2$). Due to rapid transverse spin relaxation, stimulated ESE is more informative (section 2.5). Figures 7 and 8 exhibit stimulated electron spin echo envelope modulation (sESEEM) kinetics obtained for $\tau = 120$ and 168 ns, respectively. The shorter delay time corresponds to the conditions that are optimal for ^7Li resonance (section 2.5), whereas the longer delay time was chosen to suppress the corresponding contribution. The residual high-frequency oscillations (Figure 8) clearly originate from ^1H or ^{19}F nuclei (that have similar NMR frequencies). Figure 9 exhibits modulus FT sESE (stimulated electron spin echo) spectra obtained under different excitation conditions. The predominant feature originates from ^7Li , but one also observes ^6Li satellites. The “split” line at 15 MHz originates from weakly coupled nuclei, and the peak frequencies correspond to NMR frequencies for free ^1H and ^{19}F nuclei.

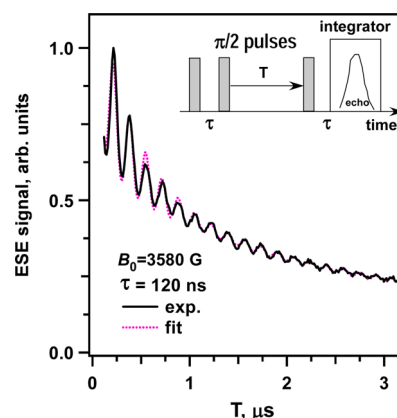


Figure 7. Like Figure 6, for stimulated electron spin echo. Time interval $\tau = 120$ ns between the first two microwave pulses corresponds to the optimal excitation of NMR transitions in matrix ^7Li nuclei.

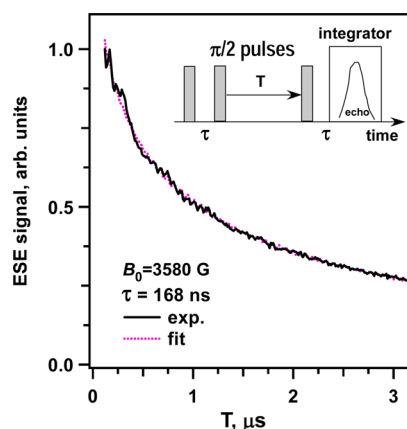


Figure 8. Like Figure 7, for time interval $\tau = 168$ ns that corresponds to the optimal suppression of NMR transitions in matrix ^7Li nuclei. The residual oscillations originate from ^1H and ^{19}F nuclei.

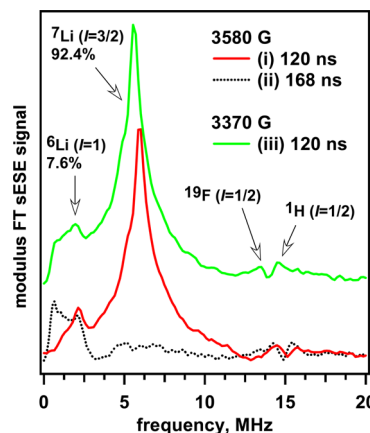


Figure 9. Modulus Fourier transform of stimulated electron spin echo kinetics obtained for the $m_1 = -1/2$ line at (i) $\tau = 120$ and (ii) $\tau = 168$ ns and the $m_1 = +1/2$ line at (iii) $\tau = 120$ ns. (See the plot legend.) Attributions of the lines to specific nuclei are given in the plot.

It follows from these ESEEM spectra that Mn^{2+} cannot reside in the LiF phase, as in such a case there would be deep modulation of the electron spin echo by ^{19}F nuclei in this matrix. This is also suggested by analysis of XAS spectra for Mn^{2+} ion in the delithiated samples (section 3.1). For the same

reason (lack of strong ^1H modulation) one can exclude the organic matrix, which narrows the choice of the host matrix to Li–C–O minerals: lithium oxalate and carbonate. The important observation is that both lithium isotopes have $I > 1/2$, so there is a quadrupolar interaction (that corresponds to the $\mathbf{I} \cdot \mathbf{Q} \cdot \mathbf{I}$ term in the spin Hamiltonian). This interaction splits resonance lines for $Q \neq 0$; however, no such splitting is apparent in our ESEEM spectra. For ^7Li , this interaction can be obscured by line broadening, but for ^6Li , the NMR frequency is low, and the effect would be readily observed. This analysis suggests that for the magnetically coupled Li^+ cations $Q \approx 0$, which is possible only if the electric field around the nucleus is nearly symmetrical; i.e., the Li^+ ion is tetrahedrally coordinated. Our examination of the reported crystal structures for lithium carbonate⁴³ and oxalate⁴⁴ (see Figure 16S, SI) indicates that while Li^+ is in a tetragonal site in the carbonate (all of the O–Li–O angles are within 5° from 110° and all of the Li–O bond lengths are close to 2 Å), in the oxalate, Li^+ is in a trigonally distorted site (the O–Li–O angles are 81° , 89° , 95° , and 128°). This consideration suggests that Mn^{2+} ion is associated specifically with the lithium carbonate phase.

To make further structural inferences, we used structural models to interpret the data that are common in the analyses of ESEEM spectra. We divided the magnetic nuclei into two groups: the nuclei in the first coordination shell (that are strongly coupled to Mn^{2+} ion) and “matrix” nuclei that are sufficiently far away that their NMR frequencies are close to those for fully decoupled (free) nuclei. We further assume that N strongly coupled nuclei of each kind are magnetically equivalent and reside at the same distance r from the ion and there is no correlation between their positions (Figure 10a). A

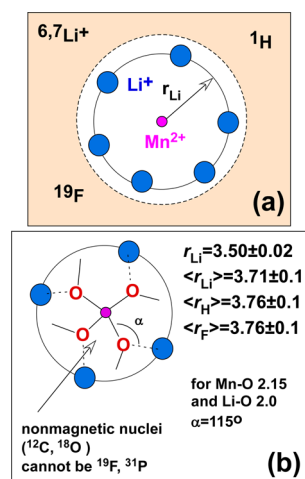


Figure 10. Models for the Mn^{2+} ion center. (a) The general model involving N equivalent $^6,^7\text{Li}^+$ ions in the first coordination shell at the fixed distance r_{Li} and “matrix” (weakly coupled) ^1H , $^6,^7\text{Li}$, and ^{19}F nuclei. (b) A more refined model of the same center with the model parameters obtained from the analyses of ESEEM kinetics and spectra. All distances are given in angstroms. The interior nuclei can only be nonmagnetic, such as oxygen-18.

point-dipole approximation for anisotropic hfc tensors is assumed for all of these nuclei. Finally, we neglect the quadrupolar terms (see above). With these assumptions, it is impossible to determine the distances to individual matrix nuclei; rather, one obtains the mean distance $\langle r \rangle$, which is

defined as $\langle r \rangle^{-6} = \sum r_i^{-6}$, where the summation is over all matrix nuclei of a given kind.

Using the standard equations for the $S' = 1/2$ system given in ref 34, from Figure 8 we estimated that for matrix ^1H and ^{19}F nuclei $\langle r \rangle \approx 3.76 \pm 0.10$ Å. In this preliminary analysis of sESEEM kinetics shown in Figure 7, we neglected contributions of all nuclei other than ^7Li , and estimated $N = 4$, $r_{\text{Li}} \approx 3.50 \pm 0.02$ Å, and $\langle r_{\text{Li}} \rangle \approx 3.71 \pm 0.05$ Å. For pESE kinetics shown in Figure 6, an improved fit was obtained by assuming $N = 6$ and $r_{\text{Li}} \approx 3.56 \pm 0.30$. As a last step, these estimates were refined in a model including all of the nuclei (Figures 17S and 18S, SI), which suggests that four Li^+ ions are sufficient to account for the pESE modulation pattern when contributions from other magnetic nuclei are taken into account (Figure 17S, SI). The same choice of model parameters reproduced the FT sESE spectra for all excitation conditions (Figure 18S, SI). These parameters are summarized in Figure 10b. Assuming that Li^+ ions are bridged to Mn^{2+} through oxygens and Li–O and Mn–O distances of 2.0 and 2.15 Å, respectively (the latter indicated by XAS), the Mn–Li distance of 3.71 Å corresponds to a Li–O–Mn angle of 113° , which is close to being tetrahedral. We emphasize that no other magnetic nuclei (^{19}F , ^{31}P) are present in the first coordination shell (see also Zhan et al.¹ and section 3.1).

Assuming that ^{19}F coupling originates through a distant PF_6^- anion (with a crystallographic P–F distance of 1.60 Å) with random orientation, the Mn–P distance can be estimated (Figure 19S, SI). Our analysis gave $\langle r_{\text{F}} \rangle \approx 3.76$ Å, which corresponds to a mean Mn–P distance of 5.5 Å; this value is too long for the ^{31}P nucleus to contribute to the sESEEM spectrum. In solution, the mean distance is given by $0.554n^{-1/3}$, where n is the number density; for 1.2 M LiPF_6 , this gives an estimate of 6.2 Å; i.e., the PF_6^- anion appears to be only slightly closer to the Mn^{2+} ion than on average, and there are no specific interactions other than charge compensation of the surface.

The intermediate conclusion is that Mn^{2+} ion resides on the surface of some Li–C–O crystallites, where this anion magnetically interacts with the nearby PF_6^- anion(s) and organic molecules (the source of the “matrix” ^1H nuclei). Lithium carbonate seems to be the most likely site for these Mn^{2+} ions. As Mn^{2+} is octahedrally coordinated, whereas Li^+ is tetrahedrally coordinated, additional ligands are necessary to complete the coordination sphere. We can exclude water and bicarbonate anion as these extra ligand(s), as that would result in strongly coupled protons, which are not observed. It seems more likely that either the solvent or the product of its electrolytic breakdown (serving as a chelating agent) completes the coordination shell. We will continue our analysis of the structure in section 4.1.

3.5. Mn^{2+} Ion Center on Li_2CO_3 : A Model System. As seen from the above, it appears that Mn^{2+} ion center in the delithiated graphite electrode is closely associated with the lithium carbonate phase; therefore, we decided to examine the Mn^{2+} -doped Li_2CO_3 already discussed in section 3.4 using ESEEM. As seen from the cw EPR spectra shown in Figures 10S and 20S (SI), the spectrum observed at 10 K is a combination of a broad line from the antiferromagnetic MnCO_3 phase and dispersed Mn^{2+} ions. When the primary spin echo is obtained (Figure 20S, to the right, SI), the EPR signal from the MnCO_3 phase is not observed, as the spin relaxation is so rapid that the magnetization decays within the dead time of the EPR spectrometer. This observation means

that the EPR signal from dispersed Mn^{2+} ions can be studied by pulsed EPR without interference from MnCO_3 . We used the same transitions that we used for Mn^{2+} ion centers on delithiated graphite electrodes in section 3.4 (indicated by the vertical arrows in Figure 20S, SI).

In Figure 21S (SI), we compare the primary ESE kinetics for Mn^{2+} ion centers on graphite and lithium carbonate. The two traces are strikingly similar. Figure 22S (SI) demonstrates FT sESEM spectra. There is a strong signal from ^6Li and also considerable proton modulation. When ^7Li modulation is suppressed (Figure 22S, SI) the kinetics are best fit by (weakly coupled) matrix protons with $\langle r_{\text{H}} \rangle = 3.27 \pm 0.03 \text{ \AA}$. For ^7Li modulation enhancement, in both fields we obtained $r_{\text{Li}} = 3.64 \pm 0.02 \text{ \AA}$ for four equivalent Li^+ ions. Addition of matrix Li^+ ions did not improve the quality of the fit. In contrast, pESEM kinetics were better simulated using five ions with $r_{\text{Li}} = 3.48 \pm 0.02 \text{ \AA}$ (see Figures 23S and 24S, SI). It appears that the structure of this Mn^{2+} ion center is less defined than that for the Mn^{2+} ion center on the delithiated graphite electrode, but the Li^+ ion shell is similar. The most striking feature of the Mn^{2+} -doped Li_2CO_3 center is deep proton modulation.

This modulation cannot originate in aqua or bicarbonate ligands, as it would be too strong; these are matrix (i.e., weakly coupled) protons, so there should be several of them to add to the observed modulation cumulatively. This analysis indicates that the observed pattern is from a *surface Mn^{2+} ion center that retains organic ligand(s)*. In this case (unlike the case with the Mn^{2+} ion center in the delithiated graphite electrode), the ligand is known; it is acetate. Using structural modeling (Figure 25S, SI) we determined that for bidentate binding, two acetate ligands would give exactly $\langle r_{\text{H}} \rangle = 3.27 \text{ \AA}$, while for monodentate binding $\langle r_{\text{H}} \rangle = 2.63$ and 2.95 \AA for one and two ligands, respectively. Thus, depending on the binding mode, either one or two acetate ligand(s) would suffice to account for the experimentally observed ^1H modulation.

The import of this section is that even in this model system the Mn^{2+} ion center is a *surface* center. Like the Mn^{2+} ion center in the delithiated graphite electrode, it involves four or five tetragonally coordinated Li^+ cations (from the crystallite surface) at distances of 3.5 – 3.64 \AA and retains organic ligands.

3.6. "Wet" Chemical Experiments. In this section we use "wet" experiments to establish which SEI phase hosts the Mn^{2+} ion in delithiated graphite electrodes using purely chemical means.

It can be expected that excess water removes all mineral phases with embedded Mn^{2+} ions, as all of these minerals have finite solubility in water. Nevertheless, neither water nor an aqueous detergent solution (0.1 wt % Triton X-100) were capable of removing Mn^{2+} ions from the graphite electrode. In these experiments, the graphite powder was first vortexed for 5 min, and then the dispersion was sonicated for an additional 10 min. We did not observe Mn^{2+} ions transferred to the aqueous solutions, nor did we observe the disappearance of EPR signal from Mn^{2+} ions in the solid material. This observation argues against the location of the Mn^{2+} ions in the organic component of the SEI, as the latter readily hydrolyzes.^{20,45,46}

In the next trial, we exposed the electrode material to (separately) aqueous solutions containing 1 M HCl and 2.5 M KCl (respectively Figures 26S and 27S, SI). In both cases, all Mn^{2+} ions were removed from the delithiated graphite material, even after a brief contact with the solutions. Finally, we used neat (glacial) acetic acid, which (like 1 M HCl) vigorously reacts with Li_2CO_3 , releasing CO_2 , while it does not dissolve

lithium oxalate and lithium fluoride (as can be shown in experiments with macroscopic samples). This treatment removed ca. 50% of the Mn^{2+} ions (Figure 28S, SI). The residue was washed with methanol and then treated with (i) an aqueous detergent solution and (ii) 1 M HCl. Once again, this neutral aqueous solution did not remove any Mn^{2+} ions, while the acidic solution removed all of the remaining Mn^{2+} ions.

The fact that water alone does not remove Mn^{2+} ions argues against the association with the oxalate phase, which is very soluble in water (the solubilities of lithium fluoride, oxalate, and carbonate in room-temperature aqueous solutions are 2.7, 80, and 15 g/L). On the other hand, the fact that 50% of the ions can be removed by neat acetic acid suggests that at least some Mn^{2+} ions are contained in the Li_2CO_3 phase that can be accessed and digested by this organic acid. The effects of HCl and KCl are noteworthy, because these reagents facilitate LiF dissolution through halide exchange.

Many authors^{17,18,47–49} have suggested that crystalline grains of different composition are interspersed in the inner SEI layer. Experiments with bulk materials indicate that acetic acid dissolves only the accessible lithium carbonate crystallites; it cannot reach the crystallites that are surrounded by LiF crystallites, blocking the access for the acid. Only when LiF crystallites are fully dissolved then can these lithium carbonate crystallites be destroyed by acidolysis. Our "wet" chemical experiments indicate that deposition of Mn^{2+} ions on the Li_2CO_3 crystallites is concomitant with the formation of LiF crystallites interspersed with these host crystallites. This process embeds the Mn^{2+} ions into the mineral component of the SEI.

3.7. Are There Mn(0) Clusters on the Lithiated Graphite? As discussed in the Introduction, one current view on the nature of deposited Mn is that it forms metallic (nano)particles. As shown in previous sections, such a view is not consistent with the EPR measurements. This leaves the possibility that reduced Mn is contained as Mn(0) in small sized clusters (of a few atoms), whose magnetic properties are different from the bulk metal and/or Mn nanoparticles. However, when summed over their different conformations and spin states, even such small Mn_n clusters are, in fact, paramagnetic.^{50,51} Therefore, these candidate Mn_n clusters must occur in particular sizes and geometries to account for our EPR results. Near complete uniformity of the Mn(0) clusters seems unrealistic. To compound this difficulty, small diamagnetic clusters have a low exchange coupling constant, and their paramagnetic excited states are readily observed using EPR above 10 K.⁴² To complement our EPR measurements (that are based on nonobservation of the expected features, as opposed to direct observations) we turned to EXAFS spectroscopy.

We remind the reader that in α -Mn(0), the unit cell consists of four distinct sites with the coordination numbers (CNs) of 16 ($\times 2$), 16 ($\times 2$), 13 ($\times 24$), and 12 ($\times 24$) that corresponds to the mean CN of 13.1 with the Mn–Mn distances between 2.24 and 2.91 \AA and with the mean Mn–Mn distance of 2.64 \AA .⁵² In gas-phase Mn_n clusters, the mean Mn–Mn bond distances are considerably longer than this crystallographic mean, based on the calculations of Jellinek et al.,⁴⁰ as shown in Figure 30S (SI). For the best-studied Mn_2 cluster, the Mn–Mn distance over 3.5 \AA is supported both by EPR in a solid matrix⁴² and by ab initio calculations in the gas phase.⁴¹ For small Mn_n clusters ($n = 5$ –8), the average Mn–Mn bond distances are 2.80–2.95 \AA .⁴⁰ For $n < 13$, the geometries of these clusters correspond to the filling of an icosahedron by facet-

joined tetrahedral units, and the trends on the gradual increase in the average CN and the concomitant decrease in the average bond lengths with the cluster size continue all the way to the bulk metal, as indicated in Figure 30S (SI), where we plotted these parameters vs $n^{-1/3}$ and extrapolated to the crystallographic parameters for α -Mn(0).⁵² Thus, the signature feature of metallic α -Mn particles in EXAFS is the observation of a large number (12–16) of nearest-neighbor atoms at the mean distance of 2.64 Å (see Figure 31S, SI), whereas for small atomic clusters these distances are still longer, and the mean CNs are 4–7 for $n = 6$ –12. In the only known diamagnetic Mn_n cluster other than the dimer ($n = 8$), the mean coordination number is 4.75 and the bond distances are 2.76–2.98 Å (see the simulated EXAFS spectrum for this cluster in Figure 31S, SI).

Figure 11a exhibits Mn K-edge EXAFS spectrum in k -space for lithiated anode, and Figure 11b demonstrates the Fourier

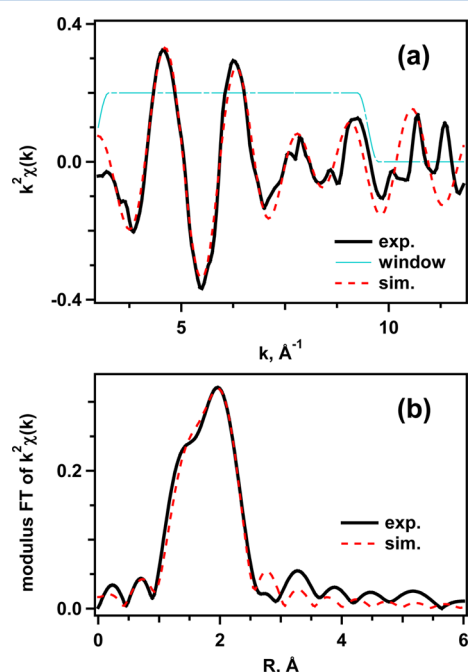


Figure 11. In panel a, the solid line is the manganese K-edge k^2 -weighted EXAFS (in the wavenumber space) of lithiated graphite electrode obtained within 3 h after harvesting of the sample. In panel b, the modulus Fourier transform of this trace is shown (obtained with the modified Hanning window indicated in panel a). Dashed lines in these two panels are simulated traces obtained using the model parameters given in the text.

transform of this spectrum in R -space using the modified Hanning window function (k range is 3.0–9.5 Å^{−1} with 0.5 Å^{−1} sills). As seen from Figure 11b, interatomic distances for the Mn emitter (uncorrected for phase shift) are significantly shorter than the expected Mn–Mn distances in either α -Mn(0) metal (nano)particles or the gas-phase Mn_n clusters (see Figure 31S, SI, for comparison). Furthermore, our simulations for the reduced Mn species indicate that the CN is very small (<5), which would be possible only in the smallest Mn_n clusters that would exhibit the longest Mn–Mn bonds (Figures 30S and 31S, SI). We have tried to simulate these EXAFS spectra taking into account the postulated presence of the residual Mn^{2+} centers despite the fact that the latter is not indicated by our EPR measurements (section 3.2). Even in this case, short

interatomic distances and low CN were required to simulate the features observed. A simulation of the EXAFS using a Mn atom for the longer scattering path indicates that the bond length would be shorter than 2.50 Å: significantly shorter than bulk metallic Mn and much shorter than calculations for small Mn clusters.

All of these observations are inconsistent with the presence of clustered Mn(0) atoms in the sample, despite an edge position in the XANES spectra that formally corresponds to Mn(0) in an α -Mn reference sample. In other words, *there is a reduced-state Mn on the lithiated graphite electrode, but this state appears not be metallic*. In this reduced state manganese is dispersed in a matrix (just like the parent Mn^{2+} center in delithiated graphite electrode) without forming a bond with another Mn atom. The best fit shown in Figure 11b was obtained by assuming the presence of just three to five atoms in the first coordination shell at distances of 1.96 ± 0.09 Å (1–2 atoms) and 2.56 ± 0.09 Å (2–3 atoms), which could be carbon or oxygen atoms. (There could also be Li atoms that may be difficult to observe in EXAFS given the low scattering cross section for this very light element.) The fit values are quite uncertain, as the data range is limited ($\Delta k = 6$ Å^{−1} and $\Delta R = 1.4$ Å), and there are two distinct scattering paths within the R window. As the Mn–O bonds approach this range, only in the higher oxidation states (i.e., greater than +2), the analysis suggests that this reduced Mn has all-carbon neighbors. This, in turn, suggests that this reduced Mn migrates from the SEI into the graphite electrode, where it intercalates with Li^0 near the surface. As the lithium has nonzero spin, the resulting diamagnetism is rationalized assuming spin coupling between Mn and Li atoms. Another possibility is that the reduced Mn occurs in an intermediate oxidation state that is diamagnetic.

4. DISCUSSION

To summarize section 3, Mn^{2+} ion centers that are observed using EPR in delithiated graphite electrodes are dispersed in the mineral component of the inner SEI on the surface of Li_2CO_3 crystallites (sections 3.2 and 3.4). Similar surface Mn^{2+} ion centers can be produced by Mn^{2+} doping of lithium carbonate (section 3.5). Our analyses indicate that Mn^{2+} ions are *not* in/on lithium fluoride and/or oxalate crystallites or the organic outer layer of the SEI (section 3.4). Dissolution experiments indicate that the mineral phase hosting these Mn^{2+} ions is interspersed with LiF grains, as only dissolution of the latter removes the Mn^{2+} completely. XAS spectroscopy (section 3.1) indicates that in delithiated graphite electrode, only such dispersed Mn^{2+} ions are present, whereas in fully lithiated electrodes there is reduction of Mn to a diamagnetic species, and no Mn^{2+} ions are observed by EPR. EPR and XAS studies examined in sections 3.2, 3.3, and 3.7 all indicate that the reduced Mn species are not α -Mn(0) (nano)particles or smaller clusters, contrary to previous suggestions. While we cannot presently suggest a structural model for this reduced Mn center, the EXAFS spectrum indicates that manganese atoms remain dispersed and hint that they reside in or on the graphite electrode rather than the organic or mineral component of the SEI. Whatever the Mn site, it clearly is electrochemically active, since the oxidation state and speciation change with insertion and removal of lithium from the electrode. We can also exclude the formation of antiferromagnetic Mn^{2+} phases, such as MnO , MnF_2 , and $MnCO_3$, on the graphite electrodes, regardless of their lithiation state. We suggest that reports of Mn(0) nanoparticles by electron microscopy could be an artifact of

Mn²⁺ reduction in focused electron beams. We proceed to discuss structural and mechanistic implications of these findings.

4.1. The Structure of Mn²⁺ Ion Center. In section 3.4, a sketch of the Mn²⁺ ion center was introduced. This spin center is located on the surface of Li–C–O compound and involves a nearby PF₆[−] cation(s). Because only lithium carbonate has tetragonal sites for Li⁺ (suggested by the absence of quadrupolar structure in ⁶⁷Li resonances), we suggest this mineral as the candidate compound, and “wet” experiments given in section 3.6 strengthen this association. Each Li⁺ cation in the Li₂CO₃ crystal has six nearby Li⁺ cations at distances between 2.70 and 3.15 Å (the mean r_{Li} ≈ 2.97 Å); for matrix ions with $r_{\text{Li}} > 3.5$ Å, direct averaging yields $\langle r_{\text{Li}} \rangle \approx 2.69$ Å. It is clear from these estimates (as well as nonzero magnetic coupling to ¹H and ¹⁹F) that Mn²⁺ ion cannot occupy an internal site in this crystal, as that would yield much stronger modulation by the matrix Li⁺ cations than what is observed experimentally ($\langle r_{\text{Li}} \rangle \approx 3.71$ Å) (see Figure 10b). Longer Li–Mn distances in the first Li⁺ ion shell (as compared to Li–Li distances in Li₂CO₃) are expected due to longer Mn–O distances and significant deviations of Mn–O–Li angles from 97° for Li–O–Li. However, it can be expected that lattice distortions beyond the second Li⁺ shell ($r_{\text{Li}} > 5$ Å) are relatively small. For a surface Mn²⁺ ion center on a Li₂CO₃ slab, this radial cutoff would be equivalent to $\langle r_{\text{Li}} \rangle \approx 3.61$ Å, which is close to the experimental estimate.

As Mn²⁺ ion is six-coordinated, there should be an organic ligand(s) that coordinates and charge compensates this surface Mn²⁺ ion, as also occurs in manganese(II) acetate doped Li₂CO₃ (section 3.5). The same is suggested by the proton modulation (Figures 6 and 7). Assuming the standard bond distances, we estimate $\langle r_{\text{H}} \rangle$ for several candidate ligands (Table 1). We remind the reader that our ESEEM analysis in section

Table 1. Estimates for $\langle r_{\text{H}} \rangle$ Mean Distance for Protons near the Mn²⁺ Ion Center

ligand	$\langle r_{\text{H}} \rangle$, Å	
	one ligand	two ligands
ethylene carbonate	4.10	3.65
ethyl methyl carbonate	3.34	2.98
–O ₂ COCH ₂ CH ₂ OCO ₂ –	3.61, ^a 3.94, ^b 4.19 ^c	–
–O ₂ COCe ^t	3.90	–

^aFolded arm. ^bExtended arm. ^cBidentate complexation.

3.4 gave an estimate of $\langle r_{\text{H}} \rangle \approx 3.76$ Å. For our estimation, we first assumed that Mn²⁺ ion forms a bond with the C=O oxygen in the solvent molecules (Figure 29S, SI). As seen from Table 1, two EC ligands or a single EMC ligand can account for the observed modulation. So do certain known products of electrochemical breakdown of the carbonate solvent, such as ethylene dicarbonate (EtOCO₂[−]) and ethyl carbonate [(–O₂COCH₂)₂; see Table 1] that contain ionized carboxyl groups. Our view of the Mn²⁺ ion center, therefore, is an octahedral complex of Mn²⁺ ion on a surface of a Li₂CO₃ crystallite, in which the coordination shell is completed either by a solvent molecule or a carboxylate product of electrochemical reduction of this solvent; the crystallite surface is charge compensated by hexafluorophosphate anions.

4.2. Mechanistic Implications. The very existence of such a specific Mn²⁺ ion center poses a challenge to the existing

scenarios for Mn deposition. The current view is that solvated Mn²⁺ ion is transported along the field lines from the positive electrode to the graphite electrode and then randomly deposited into the SEI (Figure 12a). Indeed, (i) in situ XAS

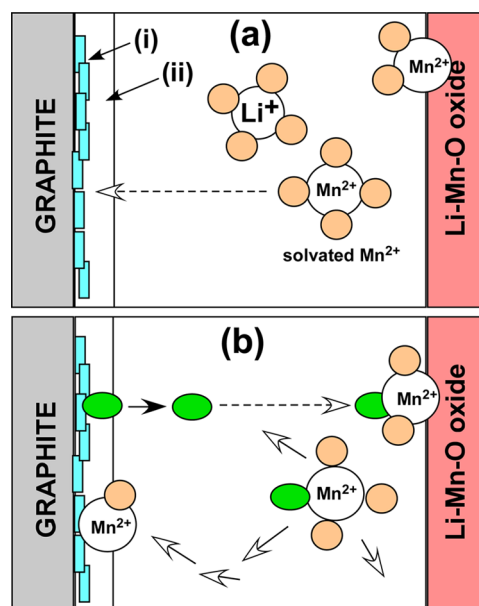


Figure 12. Two models of transport and deposition of Mn²⁺ ions in Li-ion batteries. (a) Mn²⁺ ions are solvated by carbonate molecules in the same fashion as Li⁺ ions and drift along the field lines penetrating through the outer (organic) SEI (ii) and become deposited into the inner (mineral) SEI layer at the graphite particle surface (i). (b) Electrolyte decomposition products with chelating groups reach the positive electrode and form neutral complexes of Mn(II) that diffusively migrate to the graphite surface, bypassing the outer SEI, and these complexes become chemisorbed on the surface of lithium carbonate crystallites in the inner SEI layer that serves as an ion exchanger.

spectra of Mn in electrolyte solution suggest that it is Mn²⁺ ion,¹⁰ and (ii) the same Mn species are observed in SEI whether Mn originates from a positive electrode or through intentional doping of the electrolyte with Mn²⁺ (e.g., ref 27). It appears certain that Mn²⁺ ions comprise the transported entity.

However, in such a case, it is unlikely that Mn²⁺ ions are deposited only in one of the several mineral phases occurring in the inner layer of the SEI. Within this framework, the only plausible rationale for this preference would be that Mn²⁺ ions become trapped in the organic component in the outer layer of the SEI that subsequently becomes mineralized, converting specifically to the Li₂CO₃ phase. The conceptual weakness of this rationale is 3-fold. First, it is difficult to explain why such Mn²⁺ ions would always involve an organic ligand, as suggested by our ESEEM spectra. The second difficulty is explaining the Mn²⁺ ion transport itself. As the outer (organic) SEI layer consists of molecules and polymers having free –OCO₂[−]Li⁺ groups, this layer should serve as an efficient ion exchanger, immobilizing Mn²⁺ ions moving across this layer to the electrode surface. As the resulting complexes would become electrically neutral, it is not clear how Mn²⁺ ions would ever reach the inner (mineral) SEI layer unless the outer SEI layer eventually mineralizes (which could occur ex situ during sample handling). Third, Mn²⁺ first needs to be removed from a strongly binding positive electrode surface.

An alternative scenario (Figure 12b) that has not been discussed in the literature is as follows: Mn^{2+} ion becomes chelated before or during transport. Oxidation and reduction of the carbonate solvent yield chelating carboxylated (di)anions (such as oxalate, carbonate, and ethylene dicarbonate) that would form very stable complexes with Mn^{2+} ions, explaining how the latter are removed from the positive electrode surface. As the resulting complexes are neutral, the transport of Mn^{2+} ions to the graphite electrode can no longer be directed by the electric field; it is purely diffusional. This naturally accounts for the observed preferential chemisorption of Mn^{2+} ions on certain mineral surfaces. Indeed, only strongly chelating surfaces (e.g., carbonate) would be capable of replacing these already strongly chelating ligands in the tentative transport complex, immobilizing the Mn^{2+} ion. Our conjecture also explains how migrating Mn penetrates the outer SEI layer without immobilization via ion exchange. Indeed, if Mn^{2+} ion is already chelated by carboxylated ligands, only species that are still stronger chelators can displace these ligands, and such groups are present only in the inner SEI.

This scenario has implications for developing strategies for retarding undesired capacity fade, as it suggests that in itself a loss of Mn from the positive electrode may not be problematic; it becomes so when Mn^{2+} ions are deposited *specifically* in the inner, mineralized SEI layer, where these Mn^{2+} ions can be further reduced. Indeed, some of our previous data suggest that Mn on the graphite electrodes does not always correlate with the extent of capacity fade,⁵³ which may indicate that it is not Mn presence per se that is important, but it is the location and the oxidation state that are critical. In particular, this reduced Mn species may subsequently react with the solvent that oxidizes it back to Mn^{2+} , and reaction products tie up more Li^+ ions in the SEI (see the Introduction). Had Mn^{2+} ions been immobilized in the *outer* SEI layer, this detrimental process would not occur. The fact that Mn^{2+} ion migrates as a neutral complex allows it to reach the inner SEI layer, where this ion is exchanged and adsorbed by mineral surfaces. Unless this Mn^{2+} ion is sufficiently close to the (lithiated) graphite surface, it cannot be reduced.

This consideration suggests that by adding strong chelators (that may increase dissolution of Mn) one can counter-intuitively *decrease* capacity fade, as such chelation may inhibit deposition of Mn in the inner SEI, where it is subsequently reduced. As such strong chelators originate through oxidative breakdown of certain battery additives (e.g., oxalateborates),^{54,55} the beneficial effect of such additives in inhibition of capacity fade then becomes rationalized.^{56,57}

4.3. Electrochemical Reduction of Manganese. Our XAS results (Figure 1 in section 3.1) and the previous research of Gowda et al.²⁷ indicate the presence of reduced Mn in the lithiated graphite electrode; our EPR results also indicate the absence of Mn^{2+} ions and phases containing them. Nevertheless, the expected EPR and EXAFS signatures of $\alpha\text{-Mn(0)}$ (nano)particles and/or smaller Mn clusters were not observed (sections 3.3 and 3.7). Had $\alpha\text{-Mn(0)}$ particles of the size reported in electron microscopy studies²⁶ been present in the sample, these features would be observed. Our EXAFS spectra for the reduced Mn (section 3.7) point to a different structure in which a single Mn atom has a low coordination number (<5) and short bond distances to light atoms.

These observations suggest that electrochemical reduction of dispersed Mn^{2+} ions in the SEI matrix (section 4.2) does not yield clustered Mn atoms. This reduction can be expected to

proceed in two stages corresponding to the removal of the two electrons. As the intermediate Mn(I) ions are diamagnetic, the resulting species would be silent in EPR; one can expect that the ion will still be bound to the original site of the Mn^{2+} center. Due to their spatial isolation, these Mn(I) ions may not undergo disproportionation that yields Mn(0) and Mn(II), which occurs when Mn(II) is chemically reduced. Considerable distortion of octahedral symmetry in the Mn(I) site can qualitatively account for the prominence of the pre-edge feature in the XANES spectrum, but explaining the EXAFS spectrum presents a challenge. Another possibility is that Mn(I) is reduced to Mn(0) and the resulting atoms (that no longer bind to the carbonate matrix) migrate to the graphite surface and cointercalate with the reduced Li^+ ions. Such a center may stay very close to the surface, as no Mn(0) graphite intercalates are known, and may even be associated with defects on this surface. Further studies are required to establish the identity of this reduced state and its possible role in cell capacity fade.

5. CONCLUDING REMARKS

In this study, we confirm previous observations suggesting that on aged (200 cycles) delithiated graphite electrodes Mn is present exclusively as Mn^{2+} ions. All of these Mn^{2+} ions are shown to be dispersed in a host matrix: no Mn-containing phases, such as MnCO_3 , are generated in the process. These Mn^{2+} ions are located at the surface of lithium carbonate crystallites in the inner SEI layer and retain organic ligand(s) that are likely to be carboxylate products of electrolyte breakdown. For lithiated graphite electrodes, there is reduction of Mn^{2+} ions to a diamagnetic species of still unknown nature. The only conclusive statements about this species are that (i) Mn is dispersed and (ii) it is not Mn(0) nanophase or clusters. The latter is suggested independently by EPR and X-ray spectroscopies.

On the strength of our structural analyses for Mn^{2+} ion center, we suggest that Mn^{2+} ions are transported to the graphite electrode not as charged solvent complexes (as is currently assumed) but rather as *neutral* complexes in which the cation is chelated by carboxylate groups in the products of electrolytic breakdown of the carbonate solvent. This complex avoids ion exchange in the outer SEI and reaches the inner SEI layer containing mineral phases, where Mn^{2+} ions are deposited on the surface of lithium carbonate crystallites. This transport places these ions in close proximity to the graphite particle surface, causing its partial reduction during the lithiation part of the cycle. We speculate that the reduced state can be Mn(I) ions residing in the parent site or Mn(0) atoms that migrate to the lithiated graphite surface and strongly bond to this surface. Identification of this reduced Mn and understanding of its chemical reactions are still a challenge. Subsequent oxidation of reduced Mn by the solvent during the delithiation part of the electrochemical cycle creates more carboxylated compounds that retain Li^+ ions in the SEI, so redox reactions of the deposited Mn^{2+} ions serve as a catalytic center for solvent breakdown. If this conjecture is correct, *Mn²⁺ ion deposition into the SEI does not necessarily cause capacity fade; it is the availability of these ions for redox reactions in the inner SEI layer that causes the problem.* Stronger chelation of Mn^{2+} ions may be able to prevent deposition of these ions specifically in this inner layer, thereby retarding the capacity fade. This rationale can account for the protective properties of certain battery additives.

■ ASSOCIATED CONTENT

■ Supporting Information

A PDF file containing a list of abbreviations and Figures 1S–31S with captions, including experimental and simulated EPR spectra. This material is available free of charge via the Internet at <http://pubs.acs.org>.

■ AUTHOR INFORMATION

Corresponding Authors

*I.A.S.: tel, (630) 252-9516; e-mail, shkrob@anl.gov.

*D.P.A.: tel, (630)252-4332; e-mail, abraham@anl.gov.

Notes

The authors declare no competing financial interest.

■ ACKNOWLEDGMENTS

I.A.S. thanks J. Jellinek, M. P. Jensen, and R. Wilson for insightful discussions and various Argonne colleagues for their constructive critique. D.A. and A.J.K. thank J. Lu, S. Gowda, and M. Bettge for valuable discussions. This work and the use of the Advanced Photon Source were supported by the US Department of Energy, Office of Science, Office of Basic Energy Sciences, Division of Chemical Sciences, Geosciences and Biosciences under contract No. DE-AC02-06CH11357. MRCAT operations are supported by the Department of Energy and the MRCAT member institutions. We thank S. Trask, B. Polzin, and A. Jansen, from the U.S. Department of Energy's (DOE) Cell Analysis, Modeling and Prototyping (CAMP) Facility, Argonne National Laboratory, for providing the electrodes used in this work. CAMP is supported by the DOE Vehicle Technologies Program (VTP) within the core funding of the Applied Battery Research (ABR) for Transportation Program. D.A. and Y.L. acknowledge support from the U.S. Department of Energy's Vehicle Technologies Program.

■ REFERENCES

- (1) Zhan, C.; Lu, J.; Kropf, A. J.; Wu, T.; Jansen, A. N.; Sun, Y.-K.; Qiu, X.; Amine, K. Mn(II) Deposition on Anodes and Its Effects on Capacity Fade in Spinel Lithium Manganate–Carbon Systems. *Nat. Commun.* **2013**, *4*, 2437.
- (2) Li, Y.; Bettge, M.; Polzin, B.; Zhu, Y.; Balasubramanian, M.; Abraham, D. P. Understanding Long-Term Cycling Performance of $\text{Li}_{1.2}\text{Ni}_{0.15}\text{Mn}_{0.55}\text{Co}_{0.1}\text{O}_2$ –Graphite Lithium-Ion Cells. *J. Electrochem. Soc.* **2013**, *160*, A3006–A3019.
- (3) Blyr, A.; Sigala, C.; Amatucci, G.; Guyomard, D.; Chabre, Y.; Tarascon, J.-M. Self-Discharge of $\text{LiMn}_2\text{O}_4/\text{C}$ Li-Ion Cells in Their Discharged State. *J. Electrochem. Soc.* **1998**, *145*, 194–209.
- (4) Komaba, S.; Kumagai, N.; Kataoka, Y. Influence of Manganese(II), Cobalt(II), and Nickel(II) Additives in Electrolyte on Performance of Graphite Anode for Lithium-Ion Batteries. *Electrochim. Acta* **2002**, *47*, 1229–1239.
- (5) Komaba, S.; Itabashi, T.; Kaplan, B.; Groult, H.; Kumagai, N. Enhancement of Li-Ion Battery Performance of Graphite Anode by Sodium Ion as an Electrolyte Additive. *Electrochem. Commun.* **2003**, *5*, 962–966.
- (6) Whittingham, M. S. Lithium Batteries and Cathode Materials. *Chem. Rev.* **2004**, *104*, 4271–4301.
- (7) Komaba, S.; Itabashi, T.; Ohtsuka, T.; Groult, H.; Kumagai, N.; Kaplan, B.; Yashiro, H. Impact of 2-Vinylpyridine as Electrolyte Additive on Surface and Electrochemistry of Graphite for $\text{C}/\text{LiMn}_2\text{O}_4$ Li-Ion Cells. *J. Electrochem. Soc.* **2005**, *152*, A937–A946.
- (8) Tsunekawa, H.; Tanimoto, S.; Marubayashi, R.; Fujita, M.; Kifune, K.; Sano, M. Capacity Fading of Graphite Electrodes Due to the Deposition of Manganese Ions on Them in Li-Ion Batteries. *J. Electrochem. Soc.* **2002**, *149*, A1326–A1331.
- (9) Lu, D.; Xua, M.; Zhou, L.; Garsuch, A.; Lucht, B. L. Failure Mechanism of Graphite/ $\text{LiNi}_{0.5}\text{Mn}_{1.5}\text{O}_4$ Cells at High Voltage and Elevated Temperature. *J. Electrochem. Soc.* **2013**, *160*, A3138–A3143.
- (10) Terada, Y.; Nishiwaki, Y.; Nakai, I.; Nishikawa, F. Study of Mn Dissolution from LiMn_2O_4 Spinel Electrodes Using in Situ Total Reflection X-Ray Fluorescence Analysis and Fluorescence XAFS Technique. *J. Power Sources* **2001**, *97–98*, 420–422.
- (11) Ochida, M.; Domi, Y.; Doi, T.; Tsubouchi, S.; Nakagawa, H.; Yamanaka, T.; Abe, T.; Ogumi, Z. Influence of Manganese Dissolution on the Degradation of Surface Films on Edge Plane Graphite Negative-Electrodes in Lithium-Ion Batteries. *J. Electrochem. Soc.* **2012**, *159*, A961–A966.
- (12) Ochida, M.; Doi, T.; Domi, Y.; Tsubouchi, S.; Nakagawa, H.; Yamanaka, T.; Abe, T.; Ogumi, Z. Effects of Electrolyte Additives on the Suppression of Mn Deposition on Edge Plane Graphite for Lithium-Ion Batteries. *J. Electrochem. Soc.* **2013**, *160*, A410–A413.
- (13) Esbenschade, J. L.; Gewirth, A. A. Effect of Mn and Cu Addition on Lithiation and SEI Formation on Model Anode Electrodes. *J. Electrochem. Soc.* **2014**, *161*, A513–A518.
- (14) Abellan, P.; Mehdi, B. L.; Paren, L. R.; Gu, M.; Park, C.; Xu, W.; Zhang, Y.; Arslan, I.; Zhang, J.-G.; Wang, et al. Probing the Degradation Mechanisms in Electrolyte Solutions for Li-Ion Batteries by in Situ Transmission Electron Microscopy. *Nano Lett.* **2014**, *14*, 1293–1299.
- (15) Aurbach, D.; Daroux, M. L.; Faguy, P. W.; Yeager, E. Identification of Surface-Films Formed on Lithium in Ethylene Carbonate Solutions. *J. Electrochem. Soc.* **1987**, *134*, 1611–1620.
- (16) Aurbach, D.; Levi, M. D.; Levi, E.; Schechter, A. Failure and Stabilization Mechanisms of Graphite Electrodes. *J. Phys. Chem. B* **1997**, *101*, 2195–2206.
- (17) Aurbach, D.; Markovsky, B.; Salitra, G.; Markevich, E.; Talyossef, Y.; Koltypin, M.; Nazar, L.; Ellis, B.; Kovacheva, D. Review on Electrode-Electrolyte Solution Interactions, Related to Cathode Materials for Li-Ion Batteries. *J. Power Sources* **2007**, *165*, 491–499.
- (18) Xu, K. Nonaqueous Liquid Electrolytes for Lithium-Based Rechargeable Batteries. *Chem. Rev.* **2004**, *104*, 4303–4417.
- (19) Tavassol, H.; Buthker, J. W.; Ferguson, G. A.; Curtiss, L. A.; Gewirth, A. A. Solvent Oligomerization During SEI Formation on Model Systems for Li-Ion Battery Anodes. *J. Electrochem. Soc.* **2012**, *159*, A730–A738.
- (20) Shkrob, I. A.; Zhu, Y.; Abraham, D. P. Reduction of Carbonate Electrolytes and the Formation of Solid-Electrolyte Interface (SEI) in Lithium Batteries. 2. Radiolytically Induced Polymerization of Ethylene Carbonate. *J. Phys. Chem. C* **2013**, *117*, 19270–19279.
- (21) Shkrob, I. A.; Zhu, Y.; Abraham, D. P. Reduction of Carbonate Electrolytes and the Formation of Solid-Electrolyte Interface (SEI) in Lithium Ion Batteries. 1. Spectroscopic Observations of Radical Intermediates Generated in One-Electron Reduction of Carbonates. *J. Phys. Chem. C* **2013**, *117*, 19255–19269.
- (22) Delacourt, C.; Kwong, A.; Liu, X.; Qiao, R.; Yang, W. L.; Lu, P.; Harris, S. J.; Srinivasana, V. Effect of Manganese Contamination on the Solid-Electrolyte-Interphase Properties in Li-Ion Batteries. *J. Electrochem. Soc.* **2013**, *160*, A1099–A1107.
- (23) Farges, F. Ab Initio and Experimental Pre-Edge Investigations of the Mn K-Edge XANES in Oxide-Type Materials. *Phys. Rev. B* **2005**, *71*, 155109 (14 pages).
- (24) Chalmin, E.; Farges, F.; Brown, G. E. J. A Pre-Edge Analysis of Mn K-Edge XANES Spectra To Help Determine the Speciation of Manganese in Minerals and Glasses. *Contrib. Mineral. Petrol.* **2009**, *157*, 111–126.
- (25) Han, Y.-K.; Lee, K.; Kang, S.; Huh, Y. S.; Lee, H. Desolvation and Decomposition of Metal (Mn, Co and Ni)–Ethylene Carbonate Complexes: Relevance to Battery Performance. *Comput. Mater. Sci.* **2014**, *81*, 548–550.
- (26) Xiao, X.; Liu, Z.; Unocic, R. R.; Baggetto, L.; Veith, G. M.; More, K. L.; Unocic, R. R. Unraveling Manganese Dissolution/Deposition Mechanisms on the Negative Electrode in Lithium Ion Batteries. *Phys. Chem. Chem. Phys.* **2014**, *16*, 10398–10402.

- (27) Gowda, S. R.; Gallagher, K. G.; Croy, J. R.; Bettge, M.; Thackeray, M. M.; Balasubramanian, M. Oxidation State of Cross-over Manganese Species on the Graphite Electrode of Lithium-Ion Cells. *Phys. Chem. Chem. Phys.* **2014**, *16*, 6898–6902.
- (28) Benetis, P. N.; Dave, P. C.; Goldfarb, D. Characteristics of ESEEM and HYSCORE Spectra of $S > 1/2$ Centers in Orientationally Disordered Systems. *J. Magn. Reson.* **2002**, *158*, 126–142.
- (29) Trask, S. E.; Li, Y.; Kubal, J. J.; Bettge, M.; Polzin, B. J.; Zhu, Y.; Jansen, A. N.; Abraham, D. P. From Coin Cells to 400 mAh Pouch Cells: Enhancing Performance of High-Capacity Lithium-Ion Cells Via Modifications in Electrode Constitution and Fabrication. *J. Power Sources* **2014**, *259*, 233–244.
- (30) Bondi, J. F.; Oyler, K. D.; Ke, X.; Schiffer, P.; Schaak, R. E. Chemical Synthesis of Air-Stable Manganese Nanoparticles. *J. Am. Chem. Soc.* **2009**, *131*, 9144–9145.
- (31) Ankudinov, A. L.; Ravel, B.; Rehr, J. J.; Conradson, S. D. Real-Space Multiple-Scattering Calculation and Interpretation of X-ray Absorption Near-Edge Structure. *Phys. Rev. B* **1998**, *58*, 7565–7576.
- (32) Ravel, B.; Newville, M. Athena, Artemis, Hephaestus: Data Analysis for X-ray Absorption Spectroscopy Using IFEFFIT. *J. Synchrotron Rad.* **2005**, *12*, 537–541.
- (33) Newville, M. IFEFFIT: Interactive XAFS Analysis and FEFF Fitting. *J. Synchrotron Rad.* **2001**, *8*, 322–324.
- (34) Dikanov, S. A.; Tsvetkov, Y. D. *Electron Spin Echo Envelope Modulation (ESEEM) Spectroscopy*. CRC Press: Boca Raton, FL, 1992.
- (35) Coffino, A. R.; Peisach, J. Nuclear Modulation Effects in High-Spin Electron Systems with Small Zero-Field Splittings. *J. Chem. Phys.* **1992**, *97*, 3072–3091.
- (36) Larsen, R. G.; Halkides, C. J.; Singel, D. J. A Geometric Representation of Nuclear Modulation Effects: The Effects of High Electron Spin Multiplicity on the Electron Spin Echo Envelope Modulation Spectra of Mn^{2+} Complexes of N-Ras P21. *J. Chem. Phys.* **1993**, *98*, 6704–6721.
- (37) Kasper, J. S.; Roberts, B. W. Antiferromagnetic Structure of α -Manganese and a Magnetic Structure Study of β -Manganese. *Phys. Rev.* **1956**, *101*, 537–544.
- (38) Patrick, L. Antiferromagnetism of Manganese. *Phys. Rev.* **1954**, *93*, 370.
- (39) Kavas, H.; Durmus, Z.; Senel, M.; Kazan, S.; Baykal, A.; Toprak, M. S. CTAB- Mn_3O_4 Nanocomposites: Synthesis, NMR and Low Temperature EPR Studies. *Polyhedron* **2010**, *29*, 1375–1380.
- (40) Jellinek, J.; Acioli, P. H.; García-Rodeja, J.; Zheng, W.; Thomas, O. C.; Bowen, K. H. J. Mn_n -Clusters: Size-Induced Transition to Half Metallicity. *Phys. Rev. B* **2006**, *74*, 153401.
- (41) Tzeli, D.; Miranda, U.; Kaplan, I. G.; Mavridis, A. First Principles Study of the Electronic Structure and Bonding of Mn_2 . *J. Chem. Phys.* **2008**, *129*, 154310.
- (42) Baumann, C. A.; Zee, R. J. V.; Bhat, S. V.; Weltner, W. J. ESR of Mn_2 and Mn_3 Molecules in Rare Gas Matrices. *J. Chem. Phys.* **1983**, *78*, 190–199.
- (43) Zemann, J. Die Kristallstruktur Von Li_2CO_3 . *Acta Crystallogr.* **1957**, *10*, 664–666.
- (44) Beagley, B.; Small, R. W. H. The Structure of Lithium Oxalate. *Acta Crystallogr.* **1967**, *17*, 783–788.
- (45) Nie, M.; Chalasani, D.; Abraham, D. P.; Chen, Y.; Bose, A.; Lucht, B. L. Lithium Ion Battery Graphite Solid Electrolyte Interphase Revealed by Microscopy and Spectroscopy. *J. Phys. Chem. C* **2013**, *117*, 1257–1267.
- (46) Xu, K.; Zhuang, G. V.; Allen, J. L.; Lee, U.; Zhang, S. S.; Ross, P. N., Jr.; Jow, T. R. Syntheses and Characterization of Lithium Alkyl Mono- and Dicarboxates as Components of Surface Films in Li-Ion Batteries. *J. Phys. Chem. B* **2006**, *110*, 7708–7719.
- (47) v. Cresce, A.; Russell, S. M.; Baker, D. R.; Gaskell, K. J.; Xu, K. In Situ and Quantitative Characterization of Solid Electrolyte Interphases. *Nano Lett.* **2014**, *14*, 1405–1412.
- (48) Aurbach, D.; Zinigrad, E.; Cohen, Y.; Teller, H. A Short Review of Failure Mechanisms of Lithium Metal and Lithiated Graphite Anodes in Liquid Electrolyte Solutions. *Solid State Ionics* **2002**, *148*, 405–416.
- (49) Aurbach, D. Review of Selected Electrode-Solution Interactions Which Determine the Performance of Li and Li Ion Batteries. *J. Power Sources* **2000**, *89*, 206–218.
- (50) Knickelbein, M. B. Experimental Observation of Superparamagnetism in Manganese Clusters. *Phys. Rev. Lett.* **2001**, *86*, 5255–5257.
- (51) Knickelbein, M. B. Magnetic Ordering in Manganese Clusters. *Phys. Rev. B* **2004**, *70*, 014424.
- (52) Gazzara, C. P.; Middleton, R. M.; Weiss, R. J.; Hall, E. O. A Refinement of the Parameters of α -Manganese. *Acta Crystallogr.* **1967**, *22*, 859–862.
- (53) Bettge, M.; Li, Y.; Sankaran, B.; Rago, N. D.; Spila, T.; Haasch, R. T.; Petrov, I.; Abraham, D. P. Improving High-Capacity $Li_{1.2}Ni_{0.15}Mn_{0.55}Co_{0.1}O_2$ -Based Lithium-Ion Cells by Modifying the Positive Electrode with Alumina. *J. Power Sources* **2013**, *233*, 346–357.
- (54) Shkrob, I. A.; Zhu, Y.; Marin, T. W.; Abraham, D. P. Mechanistic Insight into the Protective Action of Bis(oxalato)borate and Difluoro(oxalato)borate Anions in Li-Ion Batteries. *J. Phys. Chem. C* **2013**, *117*, 23750–23756.
- (55) Amine, K.; Chen, Z.; Zhang, Z.; Liu, J.; Lu, W.; Qin, Y.; Lu, J.; Curtiss, L.; Sun, Y.-K. Mechanism of Capacity Fade of MCMB/ $Li_{1.1}[Ni_{1/3}Mn_{1/3}Co_{1/3}]_{0.9}O_2$ Cell at Elevated Temperature and Additives to Improve Its Cycle Life. *J. Mater. Chem.* **2011**, *21*, 17754–17759.
- (56) Zhu, Y.; Li, Y.; Bettge, M.; Abraham, D. P. Positive Electrode Passivation by LiDFOB Electrolyte Additive in High-Capacity Lithium-Ion Cells. *J. Electrochem. Soc.* **2012**, *159*, A2109–A2117.
- (57) Zhu, Y.; Li, Y.; Bettge, M.; Abraham, D. P. Electrolyte Additive Combinations That Enhance Performance of High-Capacity $Li_{1.2}Ni_{0.15}Mn_{0.55}Co_{0.1}O_2$ -Graphite Cells. *Electrochim. Acta* **2013**, *110*, 191–199.